

# Site-Specific Location Calibration and Validation of Ray-Tracing Simulator NYURay at Upper Mid-Band Frequencies

Mingjun Ying\*, Dipankar Shakya, Peijie Ma, Guanyue Qian, and Theodore S. Rappaport<sup>†</sup>

NYU WIRELESS, New York University, Brooklyn, NY, USA

\*yingmingjun@nyu.edu, <sup>†</sup>tsr@nyu.edu

**Abstract**—Ray-tracing (RT) simulators are essential for wireless digital twins, enabling accurate site-specific radio channel prediction for next-generation wireless systems. Yet, RT simulation accuracy is often limited by insufficient measurement data and a lack of systematic validation. This paper presents site-specific location calibration and validation of NYURay, NYU’s in-house ray tracer, at upper mid-band frequencies (6.75 GHz and 16.95 GHz). We propose a location calibration algorithm that corrects GPS-induced position errors by optimizing transmitter-receiver (TX-RX) locations to align simulated and measured power delay profiles, improving TX-RX location accuracy by 42.3% for line-of-sight (LOS) and 13.5% for non-line-of-sight (NLOS) scenarios. Validation across 18 TX-RX locations shows excellent RT accuracy in path loss prediction, with path loss exponent (PLE) deviations under 0.14. While RT underestimates delay spread and angular spreads, their cumulative distributions remain statistically similar. The validated NYURay advances RT validation and provides reliable channel statistics for 6G deployment.

**Index Terms**—Ray tracing, location uncertainties, wireless propagation, upper mid-band, FR1, FR3, 6G, channel modeling, site-specific prediction, measurement campaign, NYURay.

## I. INTRODUCTION

Ray tracing (RT) simulation provides deterministic wireless channel prediction for diverse applications spanning network planning, coverage optimization, interference analysis, beamforming design, and channel modeling for emerging technologies including reconfigurable intelligent surfaces and integrated sensing and communications [1]–[4]. Site-specific propagation channel prediction enables operators to optimize base station placement, predict coverage gaps, and validate network performance, which typically proves impractical to analyze empirically before deployment [5], [6]. Early work in RT demonstrated the feasibility of site-specific prediction for microcellular environments [7] and commercial potential for network design [8].

RT simulation has emerged as the cornerstone technology for deterministic wireless channel prediction, yet fundamental challenges have limited prediction accuracy since initial development in the early 1990s [7], [8]. The computational complexity of electromagnetic wave propagation modeling, combined with inaccurate material characterization and oversimplified environmental representations, created a persistent gap between theoretical promise and practical deployment [8]–[11]. As wireless networks migrate toward higher frequencies

spanning upper mid-band, mmWave, and sub-THz frequencies, RT becomes essential for accurate site-specific channel prediction, as wavelengths approach environmental feature dimensions, making propagation increasingly sensitive to geometric details and material properties [12]–[14].

Existing RT simulators face critical limitations: (1) computational bottlenecks preventing real-time predictions, (2) inaccurate modeling of propagation mechanisms including diffraction and scattering phenomena, along with insufficient measurement data for RT calibration, (3) inaccurate, inefficient, and insufficiently detailed 3D environmental representations for RT simulation, (4) inadequate material databases lacking frequency-dependent characterization, and (5) poor integration with modern AI/ML frameworks [11], [15], [16].

Computational bottlenecks have prevented widespread RT deployment despite decades of development efforts. Early work by Seidel and Rappaport [9], [10] introduced image theory and ray launching methods but struggled with computational scaling, while early attempts at real-time diffraction modeling focused on 2D parametric formulations [17]. Commercial tools like Wireless InSite and WinProp implemented GPU acceleration yet remained limited by proprietary architectures and lack of comprehensive measurement validation [5]. NVIDIA Sionna achieved significant advances through differentiable ray tracing and GPU acceleration [18], yet lacks integrated measurement data and built-in calibration mechanisms for real-world validation against actual propagation measurements. Recent academic efforts achieved further speedups through novel data structures [19], real-time GPU rendering [20], and CPU/GPU heterogeneous parallelism achieving over 650× acceleration [21]. However, speed improvements often sacrificed accuracy by omitting higher-order reflections, diffraction, or scattering mechanisms, while critically lacking systematic calibration against measured channel data essential for upper mid-band frequencies and above, motivating our pursuit of a real-time RT solution with comprehensive physics.

Location uncertainty fundamentally undermines RT calibration accuracy, even with advances in material characterization methods. Traditional RT calibration approaches minimize differences between measured and simulated channels through material property adjustment [18], [22], yet ignore uncertainty in recorded transmitter and receiver locations. Measurement campaigns typically rely on consumer-grade GPS systems

that introduce as much as 5-10 meter location errors [23], undermining calibration accuracy and channel model validation. Existing commercial tools and academic frameworks lack integrated functionality for handling location uncertainty [18], [24]. To address location uncertainty, this paper introduces a systematic location calibration methodology that aligns measured and RT-simulated omnidirectional power delay profiles through multi-component loss function optimization.

Environmental modeling accuracy for site-specific environments determines RT simulation performance and remains a major constraint. Modeling approaches have evolved from simple geometric primitives to detailed 3D representations, with commercial AutoCAD-based solutions dominating early implementations [5], [25]. Modern approaches leverage open-source tools such as Blender and automated generation from databases like OpenStreetMap [1], [26], but lack comprehensive material assignment capabilities. The challenge of integrating accurate environmental modeling with comprehensive propagation physics extends beyond geometry to the underlying wave propagation mechanisms, where most RT simulators implement only basic reflection and penetration, neglecting diffraction and scattering mechanisms essential for accurate RT prediction [11].

Material characterization remains inadequately developed for upper mid-band frequencies despite recent advances. Initial RT implementations relied on generic material properties, resulting in errors exceeding 20 dB [15]. Systematic measurement-based characterization established methodologies for implementing frequency-dependent material databases in RT simulations [5], [25], [27], with recent advances extending calibration techniques to mmWave and sub-THz bands [22]. However, upper mid-band frequencies remain undercharacterized due to limited measurement campaigns [28], [29].

High-fidelity measurement datasets are essential for validating RT tools and constructing accurate propagation models. Such datasets enable rigorous benchmarking of simulation accuracy, facilitate calibration of propagation mechanisms, and support the development of robust, generalizable channel models across diverse environments and frequency bands. NYU WIRELESS measurement campaigns provide comprehensive validation datasets across multiple frequency bands essential for RT development. Extensive campaigns at 28 GHz, 73 GHz, and 142 GHz since 2012 enabled development of statistical models including NYUSIM and provided calibration data for the original NYURay simulator [22], [30]–[36]. Recent upper mid-band spectrum allocation motivated new measurement campaigns at 6.75 GHz and 16.95 GHz, addressing data scarcity hindering FR1(C) and FR3 channel model development [37]–[41].

To address the fundamental limitations of computational constraints and environmental characterization, this paper presents an enhanced NYURay simulator that introduces comprehensive architectural improvements and advanced deterministic channel propagation modeling capabilities in contrast to previous NYURay endeavors [22], [42]. Advanced propa-

gation mechanisms incorporate ITU-recommended reflection and penetration models, 3D uniform theory of diffraction (UTD) [43], and frequency-dependent rough surface scattering to capture complex propagation phenomena. The modular object-oriented architecture of NYURay facilitates extensibility and customization, while native Blender integration provides a foundation for future automated 3D environment generation and material assignment workflows utilizing the comprehensive 3D creation suite, including modeling tools, material editors, and Python API for automated workflow development [44].

The main contributions are summarized as follows. First, a comprehensive description of the NYURay RT simulator employs four fundamental propagation mechanisms (reflection, penetration, diffraction, and scattering) with GPU-accelerated computation through TensorFlow integration, validated against extensive 6.75 GHz and 16.95 GHz measurements in a detailed 3D environment model of the NYU Brooklyn campus incorporating buildings and urban infrastructure. Second, a multi-step location calibration methodology reduces GPS-induced location uncertainty through alternating minimization of multi-component PDP loss functions, reducing location errors from 5-10 meters to sub-meter precision and improving strongest multipath component power prediction in PDP by 0.96 dB for line-of-sight (LOS) and 0.74 dB for non-line-of-sight (NLOS) scenarios on average. Third, validation against 18 upper mid-band urban outdoor measurement locations demonstrates that NYURay achieves PLE differences of 0.03-0.14 from measurements. Following systematic outlier detection using combined ratio and absolute difference criteria, RT and measurement cumulative distributions demonstrate enhanced statistical agreement for root-mean-square (RMS) delay spread and angular spread parameters, though RT simulations underestimate multipath richness compared to empirical observations.

## II. RESULTS

We demonstrate and validate NYURay, an enhanced Python-based RT simulator, through comprehensive measurement campaigns at upper mid-band frequencies of 6.75 GHz and 16.95 GHz. The validation encompasses location calibration methodology addressing GPS uncertainties, extensive UMi measurements across 18 TX-RX locations with separation distances from 40 to 880 meters, and systematic RT performance assessment. Results show excellent path loss prediction accuracy with path loss exponent deviations below 0.14, while revealing characteristic underestimation of delay spread and angular spread parameters. Location calibration achieves 42.28% multipath matching improvement for line-of-sight scenarios and 13.52% for non-line-of-sight conditions. Statistical validation through systematic outlier filtering demonstrates substantial distributional agreement between RT simulations and measurements, with Kolmogorov-Smirnov statistics improving by 13.5% for delay spread and up to 38.6% for angular spread parameters.

### A. Ray-Tracing fundamentals and the need for measurements and calibration

RT emerged as a fundamental technique for wireless channel modeling in the 1980s, with early applications in indoor environments [10] and later expansion to outdoor cellular scenarios [45]. RT provides deterministic channel predictions by modeling EM wave propagation through geometric optics principles, offering significant advantages over empirical models for site-specific analysis [46]. Unlike statistical models that provide average channel characteristics, RT captures specific environmental interactions enabling accurate prediction of channel parameters including path loss (PL), delay spread (DS), and angular spread (AS) for arbitrary TX-RX configurations.

NYURay, a 3D RT tool developed at NYU WIRELESS, serves as the primary simulation platform for wireless propagation across upper mid-band spectrum, mmWave, and sub-THz bands. The enhanced NYURay simulator builds upon the foundational C++ codebase, originally calibrated using extensive measurements at 28 GHz, 73 GHz, and 142 GHz [22], [36]. The enhanced simulator transitions to Python-based platform, expanding beyond basic reflection and refraction to incorporate frequency-dependent propagation mechanisms including diffraction and scattering, guided by ITU recommendations [43]. A key contribution includes development of an interactive GUI leveraging the NYU standardized point-data format [41] to enable direct comparison between empirical measurements and simulation outputs. The point-data format represents detailed, site-specific information for each TX-RX pair, including key channel statistics (PL, DS, AS). The GUI integrates tools for statistical analysis of channel parameters and provides precise, site-specific validation of RT predictions against measured ground truth.

NYURay simulates wireless propagation by modeling EM wave interactions with the environment. For TX and RX in a propagation environment containing obstacles, NYURay traces rays from TX and calculates various paths to RX through reflection, penetration (transmission), diffraction, and scattering mechanisms.

For each individual propagation path  $p$ , NYURay computes the electric field contribution  $\mathbf{E}_p(\mathbf{r}_R)$  at RX location  $\mathbf{r}_R$  using:

$$\mathbf{E}_p(\mathbf{r}_R) = \frac{\lambda}{4\pi} \cdot \frac{e^{-jkd_p}}{d_p} \cdot \mathbf{F}_R \cdot \mathbf{T}_p \cdot \mathbf{F}_T \cdot \mathbf{E}_0 \quad (1)$$

where  $\lambda$  represents wavelength and  $k = 2\pi/\lambda$  denotes wavenumber. The total path length equals  $d_p$ , while  $\mathbf{E}_0$  represents the initial complex electric field vector. Matrices  $\mathbf{F}_T$  and  $\mathbf{F}_R$  characterize TX and RX antenna field patterns in departure and arrival directions. The cumulative transition matrix  $\mathbf{T}_p$  encapsulates all electric field transformations along the path. The expression  $\frac{e^{-jkd_p}}{d_p}$  accounts for free-space PL and phase shift, while  $\frac{\lambda}{4\pi}$  relates far-field radiation to source characteristics.

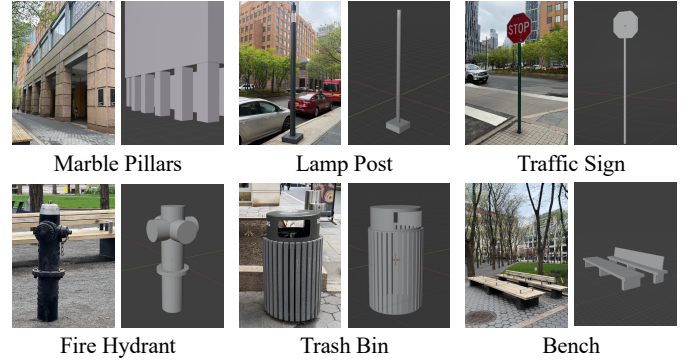


Fig. 1: Comparison of real environmental objects and corresponding 3D models in UMi measurement area. Objects include marble pillars, lamp posts, traffic signs, fire hydrants, trash bins, and benches. Additional urban facilities such as transformers, trees, and other environmental objects not shown were included in the comprehensive 3D environmental model for NYURay RT simulation, using precise locations and dimensions from field measurements.

The total electric field at RX combines contributions from all propagation paths through coherent vector summation, expressed in the Master Propagation Equation:

$$\begin{aligned} \mathbf{E}_{\text{total}}(\mathbf{r}_R) = & \underbrace{\mathbf{E}_L(\mathbf{r}_R)}_{\text{LOS}} + \underbrace{\sum_{k \in \mathcal{R}} \mathbf{E}_{R,k}(\mathbf{r}_R)}_{\text{Reflected Paths}} + \underbrace{\sum_{\ell \in \mathcal{T}} \mathbf{E}_{T,\ell}(\mathbf{r}_R)}_{\text{Transmitted Paths}} \\ & + \underbrace{\sum_{m \in \mathcal{D}} \mathbf{E}_{D,m}(\mathbf{r}_R)}_{\text{Diffracted Paths}} + \underbrace{\sum_{n \in \mathcal{S}} \mathbf{E}_{S,n}(\mathbf{r}_R)}_{\text{Scattered Paths}}. \end{aligned} \quad (2)$$

where  $\mathbf{E}_L(\mathbf{r}_R)$  represents the LOS component (when unobstructed). The remaining terms incorporate paths categorized by dominant propagation mechanisms: reflection ( $\mathcal{R}$ ), transmission/penetration ( $\mathcal{T}$ ), diffraction ( $\mathcal{D}$ ), and scattering ( $\mathcal{S}$ ). Each category contributes field components  $\mathbf{E}_{R,k}$ ,  $\mathbf{E}_{T,\ell}$ ,  $\mathbf{E}_{D,m}$ , and  $\mathbf{E}_{S,n}$  respectively. The coherent vector summation captures interference effects among all paths at RX location.

NYURay implements four fundamental propagation mechanisms: (1) Reflection computed using a hybrid approach combining Shooting and Bouncing Rays [22], image-based RT, and Fresnel reflection coefficients calculated based on material properties, polarization, and incidence angle [43]; (2) Penetration modeled for waves transitioning between media with overall loss, accounting for both boundary reflections and internal absorption [43]; (3) Diffraction implemented using Uniform Theory of Diffraction [47] where rays emanate from edges along Keller cones [48] with computed diffraction coefficients dependent on incidence angle, observation angle, and edge geometry; and (4) Scattering applied for rough surfaces exceeding the Rayleigh criterion [12], with scattered energy distribution following the Lambertian pattern [49].

Accurate 3D environment models enable reliable RT simulations and subsequent TX/RX location calibration by capturing the geometric and electromagnetic characteristics of the propagation environment. For outdoor UMi 3D environment modeling, the process involves: (1) importing OpenStreetMap (OSM) geographical data—including terrain elevation and

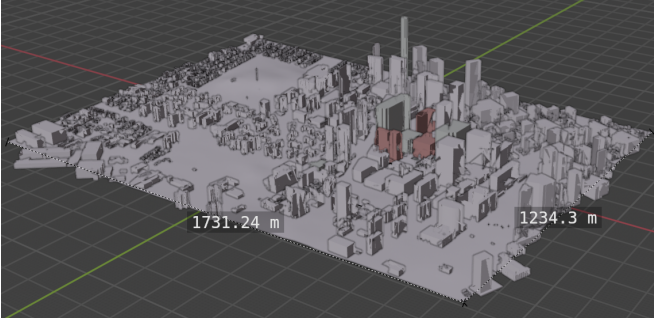


Fig. 2: 3D visualization of UMi environment model used in NYURay simulations, covering approximately  $1.2 \text{ km} \times 1.7 \text{ km}$ . Each gray grid represents  $100 \text{ m} \times 100 \text{ m}$  area. The model includes buildings, trees, lamp posts, traffic signs, benches, and fire hydrants.

building structures—using the BLOSM addon for Blender [50] to establish ground reference and basic geometry; (2) adjusting building models with laser rangefinder and iPhone LiDAR measurements to match actual dimensions, and manually creating objects such as trees, lamp posts, traffic signs, benches, and fire hydrants to enhance model fidelity (see Fig. 1 for a comparison of real objects and their 3D models); (3) assigning material properties (concrete, glass, metal, wood, marble) to object surfaces to reflect frequency-dependent EM characteristics in NYURay [43]; and (4) exporting the finalized 3D model to Mitsuba XML format for NYURay RT EM field computations.

Fig. 2 shows the isometric view of the detailed UMi 3D model. Precise geometry (building dimensions, object placement) and correct material properties minimize location calibration algorithm requirements to compensate for modeling inaccuracies. Detailed environmental features ensure simulated MPCs match real-world measurements, enabling reliable calibration results.

Environmental 3D models capture geometric details and material properties with precision for accurate EM field calculations. However, discrepancies between simulated and measured channels arise from modeling limitations, computational approximations, and environmental uncertainties. Calibration bridges the gap between theoretical predictions and real-world propagation by systematically adjusting simulation parameters to match empirical observations.

Calibration becomes essential for RT tools because: (1) theoretical scattering models may not capture all physical mechanisms in real environments; (2) material property databases contain uncertainties affecting reflection and transmission coefficients; (3) geometric approximations in 3D models introduce systematic errors; and (4) computational limitations necessitate accuracy-efficiency trade-offs. Extensive measurement campaigns provide ground truth data for validating and refining RT predictions, ensuring simulation tools deliver reliable channel characterization for wireless system design.

### B. Measurement Campaign

The NYU WIRELESS measurement campaign characterized propagation in FR1(C) and FR3 bands at 6.75 GHz and 16.95 GHz. The campaign focused on outdoor UMi, InH,

and InF environments [38]–[40], [51], [52]. Upper mid-band measurements at 6.75 GHz and 16.95 GHz were meticulously collected and processed at NYU WIRELESS.

1) *Measurement System*: The FR1(C) and FR3 measurement campaign utilized a sliding-correlation channel sounder operating at 6.75 GHz and 16.95 GHz, detailed in [39], [51]. The sounder provides 1 GHz BW, enabling 1 ns temporal resolution. Key components include dual-band co-located front-ends and steerable horn antennas (15 dBi,  $30^\circ$  HPBW at 6.75 GHz; 20 dBi,  $15^\circ$  HPBW at 16.95 GHz). Further system specifications, including PN sequence design and block diagrams, are available in [12], [39], [53], [54]. An operational EIRP of 31 dBm was maintained, providing link margins of 142.7 dB at 6.75 GHz and 143.8 dB at 16.95 GHz [38], [40]. Antennas supported V/H polarization.

2) *Measurement Data Collection Procedure*: Multipath data collection involved a two-step process: rapid RX scans to identify significant TX AODs, followed by detailed RX azimuthal sweeps in HPBW steps for comprehensive MPC capture at each TX-RX location [55]. The procedure, including five RX azimuthal sweep configurations per TX AOD and PTP synchronization using a reference MPC [56], captured data for both V-V and V-H polarizations. Omnidirectional PDPs were synthesized from directional measurements [57]. Post-processing involved applying a power threshold to directional PDPs to identify valid MPCs [58]. Each TX-RX location pair required approximately 4-5 hours for measurement.

3) *Location Recording and Positioning*: Commercial GPS technology recorded geographical coordinates of TX and RX positions throughout the measurement campaign. Location data was captured using iPhone GPS functionality through Google Earth, providing positioning accuracy of approximately 5-10 meters. GPS location uncertainty represents a fundamental limitation when correlating site-specific measurements with RT simulations, as small location discrepancies can significantly impact multipath propagation characteristics in dense urban environments.

For accurate TX-RX separation distance determination, laser ranging measurements were employed in addition to GPS location. Laser-based distance measurements provided precise TX-RX separation values independent of GPS coordinate uncertainty, ensuring accurate path loss analysis and model validation. The dual approach leveraged GPS for general positioning context while relying on laser measurements for critical distance-dependent propagation characterization.

To address GPS location logging errors and improve measurement-simulation correlation accuracy, a calibration algorithm was developed and implemented as detailed in Section II-C. The TX-RX location calibration algorithm compensates for systematic positioning errors and enhances the reliability of site-specific comparisons between measured and simulated propagation characteristics. Accurate location calibration is also important for utilizing historical measurement data for enhanced RT material parameter calibration and environment modeling.

TABLE I: Point-data statistics for UMi large-scale spatio-temporal RT simulations, spatially averaged over 25 RX locations, at 6.75 GHz and 16.95 GHz. The corresponding point-data table for UMi measurement results can be found in [38].

Freq.	TX	RX	Loc Type	TR Sep	Omni Abs. PL	Omni DS	Omni AoA 3GPP (6)	Omni AoA Fleury (5)	Omni AoD 3GPP (6)	Omni AoD Fleury (5)	Omni ZoA 3GPP (6)	Omni ZoA Fleury (5)	Omni ZoD 3GPP (6)	Omni ZoD Fleury (5)
[GHz]				[m]	[dB]	[ns]	[°]	[°]	[°]	[°]	[°]	[°]	[°]	[°]
6.75	TX1	RX1	LOS	40	77.05	13.45	14.30	15.07	15.95	18.26	6.23	6.24	3.32	3.33
		RX2	LOS	100	85.29	23.53	6.69	7.66	11.76	16.02	3.37	3.38	2.79	2.79
		RX3	LOS	193	91.29	82.08	1.19	1.64	27.60	40.30	1.91	1.91	1.65	1.65
		RX4	NLOS	561	103.55	80.72	0.46	0.48	32.47	44.71	0.42	0.42	0.88	0.88
		RX5	NLOS	880	113.59	4.06	2.44	2.45	1.33	1.98	0.81	0.81	0.44	0.44
		RX7	LOS	420	99.29	12.39	0.67	0.68	13.21	18.96	0.61	0.61	2.08	2.09
	TX2	RX1	LOS	58	82.25	14.13	17.53	17.53	15.04	18.47	2.40	2.40	3.42	3.49
		RX2	NLOS	51	84.39	55.76	25.04	29.21	18.01	19.41	4.41	4.43	3.17	3.17
		RX3	NLOS	101	102.02	22.74	19.14	19.50	2.95	2.97	2.03	2.03	0.69	0.69
	TX3	RX1	NLOS	71	124.76	68.33	13.69	13.75	4.90	4.89	1.75	1.75	1.94	1.94
		RX2	NLOS	45	100.45	12.13	2.33	2.33	17.19	18.81	0.91	0.91	0.47	0.47
		RX3	NLOS	125	117.72	1.24	0.69	0.43	0.35	0.17	0.28	0.17	0.51	0.30
	TX4	RX1	NLOS	89	102.15	98.68	22.40	23.88	41.93	49.01	2.17	2.17	3.63	3.65
		RX2	LOS	120	88.91	18.07	9.34	11.60	18.43	19.76	2.74	2.75	4.37	4.38
		RX4	NLOS	184	146.98	29.24	6.27	6.27	4.18	4.18	1.03	1.03	2.06	2.06
	TX5	RX1	LOS	52	80.53	32.78	18.55	18.91	17.80	18.29	3.90	3.90	2.39	2.39
		RX2	NLOS	167	106.99	7.93	4.41	4.42	9.61	9.70	1.10	1.10	1.71	1.71
		RX3	NLOS	141	115.64	334.65	40.97	39.50	44.61	43.08	1.83	1.83	1.82	1.82
16.95	TX1	RX1	LOS	40	85.50	10.71	12.09	12.56	13.76	15.23	6.02	6.03	2.97	2.98
		RX2	LOS	100	93.51	19.70	6.01	6.77	9.30	12.39	3.32	3.33	2.52	2.52
		RX3	LOS	193	99.56	81.79	0.87	1.13	27.02	39.60	1.94	1.94	1.38	1.38
		RX4	NLOS	561	115.53	148.37	0.54	0.56	71.04	72.83	0.46	0.46	0.93	0.93
		RX5	NLOS	880	124.40	4.00	2.16	2.17	1.19	1.85	0.77	0.77	0.39	0.39
		RX7	LOS	420	108.19	8.81	0.56	0.56	11.00	15.67	0.51	0.51	1.82	1.84
	TX2	RX1	LOS	58	90.01	13.04	19.35	19.27	11.38	13.73	2.72	2.72	2.64	2.69
		RX2	NLOS	51	94.66	69.60	26.12	29.95	18.80	20.28	4.04	4.06	3.08	3.08
		RX3	NLOS	101	110.05	21.26	18.93	19.30	2.72	2.73	2.02	2.02	0.69	0.69
	TX3	RX1	NLOS	71	136.67	61.19	14.75	14.75	6.06	6.06	1.65	1.65	2.03	2.03
		RX2	NLOS	45	108.47	10.14	2.17	2.18	18.49	20.27	0.97	0.97	0.46	0.46
		RX3	NLOS	125	130.89	0.28	0.32	0.10	0.12	0.04	0.10	0.04	0.18	0.07
	TX4	RX1	NLOS	89	110.68	97.80	19.83	21.20	35.09	44.75	2.00	2.00	2.71	2.73
		RX2	LOS	120	97.30	12.08	7.54	8.85	15.86	16.90	2.55	2.56	3.76	3.77
		RX4	NLOS	184	142.97	19.89	3.46	3.45	3.02	3.05	0.55	0.55	1.11	1.10
	TX5	RX1	LOS	52	88.68	32.27	16.79	17.24	17.59	18.02	3.85	3.85	2.20	2.20
		RX2	NLOS	167	114.58	7.93	4.23	4.24	10.06	10.24	1.17	1.17	1.73	1.73
		RX3	NLOS	141	124.80	275.08	32.01	32.33	34.61	35.35	1.61	1.61	1.46	1.47

4) *Measurement Environment*: An extensive UMi campaign was conducted around the NYU Tandon School of Engineering campus in MetroTech Commons and on a 1 km path along Myrtle Avenue [38]–[40], [51], [52]. Location provides representative dense urban microcell setting with varied building geometries and street furniture, suitable for characterizing propagation at upper mid-band frequencies. The environment included potential reflectors, scatterers, and shadowers such as lamp posts, transformers, concrete and marble pillars, trees, foliage, traffic signs, pedestrians, benches, trash bins,

and fire hydrants. Reflections were observed primarily from surrounding buildings and metal lampposts [39]. To emulate typical small-cell outdoor deployments, TXs were positioned at 4 m above ground (similar to lamppost heights, representing small-cell BS), and RXs at 1.5 m (mimicking mobile user equipment).

TX and RX locations, including TX-RX pairs in the ~180 m open-square MetroTech Commons and along Myrtle Avenue (a typical street path), are detailed and illustrated in [38]. A total of 20 locations were measured (7 LOS, 13 NLOS) with

TX-RX distances from 40 to 1000 m. Two outages at NLOS locations were observed at both 6.75 and 16.95 GHz [38].

5) *Measurement Data Processing and Point-Data Format*: A standardized point-data format addresses inconsistent data presentation and facilitates data pooling across organizations [41]. The format represents channel measurements and simulation outputs on a site-specific TX-RX link basis, retaining full data granularity for accurate environmental depiction at each location pair. Standardizing key channel parameters provides a common framework for direct comparison between empirical measurements and simulation outputs (e.g., from NYURay), enables dataset pooling, and supports statistical analysis or RT validation [41].

Rigorous calibration steps ensured amplitude and delay consistency. Daily field calibrations using a 4 m free-space PL reference corrected fluctuations in output power, oscillator settings, and synchronized Rb clocks [39]. Measurements alternated between V-V and V-H polarizations to mitigate bias and enrich MPC capture. Omni channel response was synthesized by rotating horn antennas incrementally and combining data in post-processing (removing antenna patterns, summing powers) to emulate an isotropic antenna [57].

The standardized point-data format resolves data format inconsistency across institutions. Standard noise threshold for identifying MPCs from PDPs and spatial threshold for identifying SLs from PAS are consistently implemented [39], [59]. The format embeds comprehensive metadata (antenna polarization, site-specific context) alongside raw measurements, providing a common method to display multiple statistics and pool datasets. RMS AS is provided using both 3GPP [60] and Fleury methods [61]. The framework supports pooling for future AI applications and provides machine-readable, interoperable results for validating wireless RTs.

#### Statistical Channel Parameter Computation

The point-data table values are derived from statistical characterization of key wireless channel parameters including PL, RMS DS, and RMS AS. Methodologies for computing channel statistics from measured or simulated PDPs follow standard approaches with lognormal distribution assumptions, enabling direct comparison with established 3GPP channel models [60].

*Path Loss Computation*: The CI PL model with 1 m free-space reference distance describes distance-dependent PL using PLE  $n$  and shadow fading  $\chi_\sigma$  [62]:

$$PL^{CI}(f_c, d_{3D}) \text{ [dB]} = \text{FSPL}(f_c, 1\text{m}) + 10n \log_{10} \left( \frac{d_{3D}}{d_0} \right) + \chi_\sigma, \quad (3)$$

$$\text{FSPL}(f_c, 1\text{m}) = 32.4 + 20 \log_{10} \left( \frac{f_c}{1 \text{ GHz}} \right),$$

where  $\text{FSPL}(f_c, 1 \text{ m})$  represents free-space PL at carrier frequency  $f_c$  GHz at 1 m, and  $\chi_\sigma$  denotes zero-mean Gaussian shadow fading with standard deviation  $\sigma^{CI}$  in dB.

*Delay Spread Computation*: RMS DS  $\sigma_\tau$  quantifies temporal dispersion as the square root of the second central moment

of the PDP [12]:

$$\sigma_\tau = \sqrt{\frac{\sum_{i=1}^K (\tau_i - \bar{\tau})^2 P_i}{\sum_{i=1}^K P_i}}, \quad (4)$$

where  $\bar{\tau} = \frac{\sum_{i=1}^K \tau_i P_i}{\sum_{i=1}^K P_i}$  represents power-weighted average delay,  $\tau_i$  denotes excess delay of the  $i^{\text{th}}$  MPC relative to first arrival, and  $P_i$  represents MPC power in linear scale.

*Angular Spread Computation*: RMS AS  $\sigma_{AS}$  characterizes spatial dispersion of MPCs. Two primary methods are employed: Fleury's definition and the 3GPP TR 38.901 approach.

Fleury's method [61] calculates the second central moment of the PAS:

$$\sigma_{AS}^{\text{Fleury}} = \min_{\Delta} \left[ \sqrt{\frac{\sum_{n=1}^N \sum_{m=1}^{M_n} (\theta_{n,m,\mu}(\Delta))^2 \cdot P_{n,m}}{\sum_{n=1}^N \sum_{m=1}^{M_n} P_{n,m}}} \right], \quad (5)$$

where  $\theta_{n,m,\mu}(\Delta) = \text{mod}(\theta_{n,m}(\Delta) - \mu(\Delta) + \pi, 2\pi) - \pi$  represents relative direction,  $\mu_\theta(\Delta) = \frac{\sum_{n=1}^N \sum_{m=1}^{M_n} \theta_{n,m}(\Delta) \cdot P_{n,m}}{\sum_{n=1}^N \sum_{m=1}^{M_n} P_{n,m}}$  denotes power-weighted mean angle, and  $\Delta$  represents angular shift array.

The 3GPP TR 38.901 method [60] employs circular standard deviation using complex phasors:

$$\sigma_{AS}^{3GPP} = \sqrt{-2 \times \ln \left| \frac{\sum_{n=1}^N \sum_{m=1}^{M_n} e^{j\theta_{n,m}} P_{n,m}}{\sum_{n=1}^N \sum_{m=1}^{M_n} P_{n,m}} \right|}, \quad (6)$$

where  $\theta_{n,m}$  represents angle of  $m^{\text{th}}$  MPC in  $n^{\text{th}}$  cluster with power  $P_{n,m}$ . The method eliminates phase wrapping ambiguities and computational overhead of Fleury's approach.

The point-data tables (e.g., Table I) enable site-specific analysis and statistical modeling, allowing CDF generation or curve fitting directly from the table for broader 3GPP and NGA applicability [41]. Tables include detailed RT simulation parameters including center frequency, TX/RX locations, PL (Omni Abs. PL spatially averaged over 25 RX locations), DS (Omni RMS DS), and AS (Omni RMS ASA/ASD/ZSA/ZSD). RMS AS computation uses both Fleury [61] and 3GPP methods [60]. RMS DS are calculated following the method in 3GPP TR 38.901 [60].

#### C. TX-RX Location Calibration

The TX-RX location calibration method optimizes transmitter and receiver positions by minimizing discrepancies between simulated and measured PDPs. The calibration addresses GPS-induced location uncertainty in field measurements, enhancing RT validation accuracy through systematic location refinement.

1) *Problem Formulation*: Initial TX and RX locations,  $\mathbf{p}_{TX}^{(0)}$  and  $\mathbf{p}_{RX}^{(0)}$ , derive from GPS coordinates recorded during measurements. GPS coordinates transform into local Cartesian coordinates aligned with the 3D environment model using Azimuthal Equidistant (AEQD) projection [63]. Initial z-coordinates correspond to antenna heights: 4 m for TX and 1.5 m for RX.

$$\mathbf{p}_{TX}^{(0)} = [x_{TX}^{(0)}, y_{TX}^{(0)}, z_{TX}^{(0)}], \quad \mathbf{p}_{RX}^{(0)} = [x_{RX}^{(0)}, y_{RX}^{(0)}, z_{RX}^{(0)}]. \quad (7)$$

Location optimization determines TX and RX position adjustments  $\Delta \mathbf{p}_{TX}$  and  $\Delta \mathbf{p}_{RX}$ :

$$\mathbf{p}_{TX}^* = \mathbf{p}_{TX}^{(0)} + \Delta \mathbf{p}_{TX}, \quad \mathbf{p}_{RX}^* = \mathbf{p}_{RX}^{(0)} + \Delta \mathbf{p}_{RX}. \quad (8)$$

Optimal locations minimize PDP discrepancies:

$$\{\Delta \mathbf{p}_{TX}^*, \Delta \mathbf{p}_{RX}^*\} = \arg \min_{\Delta \mathbf{p}_{TX}, \Delta \mathbf{p}_{RX}} L(P_{sim}, P_{meas}), \quad (9)$$

where  $L(\cdot, \cdot)$  quantifies differences between simulated omnidirectional PDP  $P_{sim}$  and measured omnidirectional PDP  $P_{meas}$  [38], [57].

Physical constraints limit the position adjustment search space:

$$\|\Delta \mathbf{p}_{TX}\| \leq d_{\max}, \quad \|\Delta \mathbf{p}_{RX}\| \leq d_{\max}, \quad \Delta z_{TX} = \Delta z_{RX} = 0, \quad (10)$$

where  $d_{\max} = 10$  m represents maximum adjustment based on GPS accuracy limitations [23]. Height constraints apply since vertical antenna positions are measured with laser rangefinders.

2) *RT Simulation and PDP Generation*: NYURay models EM wave propagation including LOS paths, reflections, and diffractions. For each TX-RX pair, NYURay computes paths with complex amplitudes  $a_i$  and delays  $\tau_i$ . The CIR formulation:

$$h(t) = \sum_{i=1}^{N_p} a_i \delta(t - \tau_i), \quad (11)$$

where  $N_p$  denotes path count and  $\delta(\cdot)$  represents the Dirac delta function. PDP calculation follows:

$$P(\tau) = |h(t)|^2 = \sum_{i=1}^{N_p} |a_i|^2 \delta(t - \tau_i). \quad (12)$$

3) *PDP Alignment Techniques*: Temporal alignment compensates for reference point differences and timing offsets between simulated and measured PDPs. Maximum peak alignment utilizes dominant path delays:

$$\Delta \tau_{simple} = \tau_{sim}^{\max} - \tau_{meas}^{\max}, \quad (13)$$

where  $\tau_{sim}^{\max}$  and  $\tau_{meas}^{\max}$  denote delays of maximum power in simulated and measured PDPs. For complex multipath environments, correlation-based alignment applies:

$$\Delta \tau_{multi} = \arg \max_{\Delta \tau} \text{corr}(P_{sim}(\tau), P_{meas}(\tau + \Delta \tau)). \quad (14)$$

4) *Multi-Component Loss Function*: The loss function combines specialized components evaluating PDP similarity:

**Peak Matching Loss** Peak matching aligns significant MPCs by quantifying temporal and power discrepancies:

$$L_{peak} = \frac{1}{N_{matched}} \sum_{i=1}^{N_{sim}} \min_j \left[ w_i \left( \frac{|\tau_{sim,i} - \tau_{meas,j}|}{T_{norm}} + |P'_{sim,i} - P'_{meas,j}| \right) \right], \quad (15)$$

where  $N_{matched}$  denotes matched peaks;  $w_i = e^{-\tau_{sim,i}/\tau_{ref}}$  prioritizes early paths with  $\tau_{ref} = 500$  ns;  $T_{norm} = 100$  ns

normalizes delay differences; and  $P'_{sim,i}$ ,  $P'_{meas,j}$  are normalized peak powers.

**Unmatched Peaks Penalty** Unmatched peaks penalty encourages similar MPC richness:

$$L_{unmatched} = w_{unmatched} \cdot \frac{|N_{sim} - N_{meas}|}{\max(N_{sim}, N_{meas})}, \quad (16)$$

where  $N_{sim}$  and  $N_{meas}$  represent significant peak counts in simulated and measured PDPs, and  $w_{unmatched} = 0.5$ .

**Shape Loss** Shape loss evaluates overall PDP distribution similarity:

$$L_{shape} = \frac{1}{|\mathcal{R}|} \sum_{\tau \in \mathcal{R}} (P_{sim,dB}(\tau) - P_{meas,dB}(\tau))^2, \quad (17)$$

where  $P_{dB}$  represents dB-scale power values and  $\mathcal{R}$  denotes delay bins exceeding the significance threshold.

The combined loss function with regularization:

$$L = \alpha \cdot (L_{peak} + L_{unmatched}) + (1 - \alpha) \cdot L_{shape} + \beta \cdot L_{distance}, \quad (18)$$

where  $\alpha = 0.7$  weights peak-based metrics relative to shape metrics,  $L_{distance} = (\|\Delta \mathbf{p}_{TX}\|^2 + \|\Delta \mathbf{p}_{RX}\|^2) / (d_{\max}^2)$  penalizes large TX and RX position adjustments from initial GPS coordinates, and  $\beta = 0.05$ .

5) *Location Optimization Algorithm*: The optimization employs alternating minimization, sequentially refining TX position (fixed RX) then RX position (fixed TX), reducing computational complexity from  $O(N_{grid}^4)$  to  $O(N_{grid}^2)$ . Each position optimization follows a three-step approach:

**Step 1 Coarse Grid Search**: Systematic evaluation examines candidate locations within  $[-5, 5]$  m range using 2.5 m grid spacing. For each candidate position, NYURay computes the RT simulation and evaluates the loss function  $L$ . The grid search identifies the coarse optimal region containing the loss minimum.

**Step 2 Fine Grid Refinement**: Around the coarse optimum, fine grid search employs 0.5 m spacing within  $\pm 1.5$  m range. The refined search localizes the minimum with sub-meter precision while maintaining computational efficiency.

**Step 3 Gradient-Free Optimization**: Powell's conjugate direction method [64] performs final refinement from the fine grid optimum. The method iteratively searches along conjugate directions without requiring gradient computation, suitable for the non-differentiable RT simulation function. Convergence occurs when position updates fall below 0.1 m threshold.

Algorithm 1 details the complete optimization procedure. The alternating minimization continues until both TX and RX position updates converge below the threshold  $\epsilon = 0.1$  m, typically within 3–5 iterations.

6) *Calibration Performance*: Table II presents key performance metrics for the location calibration algorithm. Across all measured T-R pairs, calibration yields average loss function reduction of 24.70%. LOS scenarios demonstrate substantial average loss reduction of 42.28%, while NLOS scenarios achieve 13.52% reduction. For LOS links, average difference between simulated and measured peak power decreases from

### Algorithm 1 TX-RX Location Calibration via Alternating Minimization

**Require:** Initial positions  $\mathbf{p}_{TX}^{(0)}, \mathbf{p}_{RX}^{(0)}$ , measured PDP  $P_{meas}$ , 3D environment model, NYURay RT engine parameters

**Ensure:** Calibrated positions  $\mathbf{p}_{TX}^*, \mathbf{p}_{RX}^*$

- 1: **Initialize:**  $\mathbf{p}_{TX} \leftarrow \mathbf{p}_{TX}^{(0)}, \mathbf{p}_{RX} \leftarrow \mathbf{p}_{RX}^{(0)}$
- 2: **Parameters:**  $d_{max} = 10$  m,  $\epsilon = 0.1$  m,  $N_{max} = 10$
- 3: **for**  $iter = 1$  **to**  $N_{max}$  **do**
- 4:    $\mathbf{p}_{RX}^{prev} \leftarrow \mathbf{p}_{RX}$
- 5:   **Step 1:** Coarse grid search
- 6:   **for**  $\Delta x \in \{-5, -2.5, 0, 2.5, 5\}$  m **do**
- 7:     **for**  $\Delta y \in \{-5, -2.5, 0, 2.5, 5\}$  m **do**
- 8:        $\mathbf{p}_{RX}^{cand} \leftarrow \mathbf{p}_{RX}^{(0)} + [\Delta x, \Delta y, 0]^T$
- 9:       **if**  $\|\mathbf{p}_{RX}^{cand} - \mathbf{p}_{RX}^{(0)}\| \leq d_{max}$  **then**
- 10:          Run RT:  $P_{sim} \leftarrow \text{NYURay}(\mathbf{p}_{TX}, \mathbf{p}_{RX}^{cand})$
- 11:          Evaluate:  $L_{cand} \leftarrow L(P_{sim}, P_{meas})$  using (18)
- 12:       **end if**
- 13:     **end for**
- 14:   **end for**
- 15:    $\mathbf{p}_{RX}^{coarse} \leftarrow \arg \min L_{cand}$
- 16:   **Step 2:** Fine grid refinement around  $\mathbf{p}_{RX}^{coarse}$
- 17:   Search  $\pm 1.5$  m with 0.5 m spacing  $\rightarrow \mathbf{p}_{RX}^{fine}$
- 18:   **Step 3:** Powell optimization from  $\mathbf{p}_{RX}^{fine}$
- 19:    $\mathbf{p}_{RX} \leftarrow \text{Powell}(L, \mathbf{p}_{RX}^{fine}, \text{tol} = 0.1)$
- 20:    $\mathbf{p}_{TX}^{prev} \leftarrow \mathbf{p}_{TX}$
- 21:   Repeat Steps 1–3 for TX optimization  $\rightarrow \mathbf{p}_{TX}$
- 22:   **if**  $\|\mathbf{p}_{TX} - \mathbf{p}_{TX}^{prev}\| < \epsilon$  **and**  $\|\mathbf{p}_{RX} - \mathbf{p}_{RX}^{prev}\| < \epsilon$  **then**
- 23:     **break**
- 24:   **end if**
- 25: **end for**
- 26: **return**  $\mathbf{p}_{TX}^* = \mathbf{p}_{TX}, \mathbf{p}_{RX}^* = \mathbf{p}_{RX}$

TABLE II: Calibration Performance Metrics Summary

Scen.	$\dagger$ Loss	Peak Power Diff. (dB)		$\ast$ Peak Power
	Reduct. (%)	Original	Calibrated	Impr. (dB)
LOS	42.28	2.44	1.48	0.96
NLOS	13.52	8.09	7.35	0.74

$\dagger$ Loss Reduct: Normalized reduction in loss function value (%) using (18).

$\ast$ Peak Power Impr.: Improvement (reduction) in absolute difference between simulated and measured peak power, comparing original RT simulation results to calibrated location results.

2.44 dB to 1.48 dB (0.96 dB improvement). For NLOS links, average difference decreases from 8.09 dB to 7.35 dB (0.74 dB improvement).

Fig. 3 illustrates calibration impact on PDP for TX1-RX4 link (560 m separation) at 6.75 GHz. RT simulation using uncalibrated locations overestimates received power by 8 dB and exhibits 4 ns temporal mismatch. RT simulation with calibrated locations reduces delay mismatch to 0.1 ns and power difference to 0.5 dB, demonstrating improved alignment with measured data. The calibration methodology effectively compensates for GPS location errors, enabling accurate site-

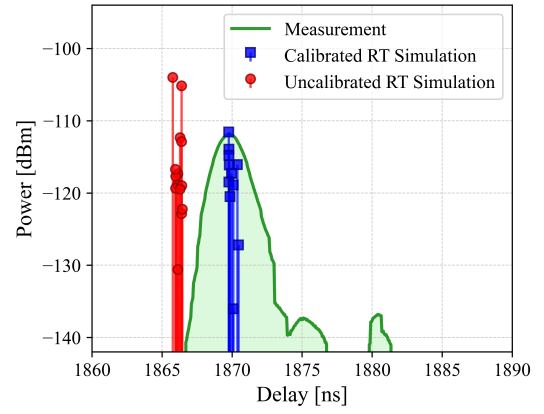


Fig. 3: PDP comparison showing measured data versus uncalibrated and calibrated location RT simulations for TX1-RX4 (560 m) in UMi environment at 6.75 GHz.

TABLE III: Key Simulation Parameters

Parameter	Value / Assumption
TX/RX Antenna Pattern	Isotropic, 0 dBi gain
Transmit Power	0 dBm
Carrier Frequency	6.75 GHz and 16.95 GHz
Minimum Considered Received Power	-160 dBm (CIR cutoff threshold)
RT Mechanisms Enabled	Reflection, Diffraction
Noise and Bandwidth Constraints	Not included (idealized CIR used)

specific channel validation.

### D. Ray-Tracing Simulation Setup for Validation

To enable direct comparison with measurement results, where omnidirectional PDPs were synthesized by removing antenna gains [57], key RT simulation parameters were configured for NYURay as summarized in Table III. Isotropic antennas with 0 dBi gain were employed at TX and RX locations, consistent with synthesized omnidirectional measurements. Transmit power was set to 0 dBm for RT simulations at 6.75 GHz and 16.95 GHz. RT simulations used 18 valid TX-RX locations from the measurement campaign, excluding TX4-RX3 and TX1-RX6 outage locations for both frequencies to maintain consistency between measured and simulated datasets.

A minimum received power threshold (CIR cutoff) of -160 dBm was established to match the practical maximum PL of approximately 160 dB [39]. The Mini-Circuits dual-band RF unit provides link margins of 142.7 dB at 6.75 GHz and 143.8 dB at 16.95 GHz with maximum EIRP of 31 dBm. The -160 dBm cutoff ensures weak MPCs remain detectable within the dynamic range. Reflection and diffraction were enabled; scattering and penetration were disabled. RT simulation employed single carrier frequency modeling narrowband channel response to focus on dominant geometric propagation paths. Noise and receiver bandwidth limitations were excluded, producing idealized CIRs.

Penetration through buildings was disabled due to unavailable detailed building structure information and substantial material penetration losses in outdoor UMi scenarios at studied

TABLE IV: RMS heights  $h_{\text{rms}}$  for common building materials [66].

Material	RMS height $h_{\text{rms}}$ ( $\mu\text{m}$ )
Wood	76.4 – 80.0
Plexiglass	8.2 – 14.5
Drywall	96.4 – 99.2
Concrete	264.3 – 269.0
Red brick	321.3 – 325.0

frequencies [39], [52]. Reflection and diffraction dominate outdoor coverage mechanisms.

Scattering effects were neglected based on the Rayleigh criterion [12], [65]. Significant diffuse scattering occurs when RMS surface height variation  $h_{\text{rms}}$  exceeds threshold height  $h_{\text{th}} = \lambda/(8 \cos \theta_i)$ , where  $\lambda$  represents wavelength and  $\theta_i$  denotes incidence angle. At normal incidence ( $\theta_i = 0^\circ$ ),  $h_{\text{th,min}} = \lambda/8$ . At 6.75 GHz ( $\lambda \approx 44.4$  mm),  $h_{\text{th,min}} \approx 5.6$  mm. At 16.95 GHz ( $\lambda \approx 17.7$  mm),  $h_{\text{th,min}} \approx 2.2$  mm.

RMS surface heights for typical building materials within the measurement environment (Table IV) satisfy  $h_{\text{rms}} \ll h_{\text{th}}$  at both frequencies. Surfaces are electrically smooth, and the Rayleigh criterion for significant diffuse scattering is not met. Scattering effects were neglected while maintaining accuracy for dominant propagation mechanisms.

NYURay employs ray launching with one million ( $1 \times 10^6$ ) rays per TX location. Ray count balances angular resolution for accurate spatial channel characteristics against computational complexity [9]. Prior convergence tests indicate one million rays provide optimal trade-off for detailed UMi environments [22]. Each TX-RX link simulation required approximately 2-3 seconds.

NYURay calculates power reduction from reflections and diffractions based on interaction geometry and material electromagnetic properties [16]. RT through the 3D environmental model (Fig. 2) accounts for interactions with buildings, ground, and modeled structures using Fibonacci lattice method. Maximum reflection depth was set to 5, allowing up to five reflections per ray sequence while capturing significant MPCs and avoiding excessive computation for highly attenuated higher-order reflections. Received power is calculated by summing contributions of all rays arriving within a receiver sphere using (2).

#### E. Site-Specific Channel Characteristics Validation for UMi at Upper Mid-Band

Building upon the location calibration, data collection, and RT simulation settings detailed in previous sections, the validation analysis examines NYURay RT tool performance against measured channel characteristics obtained in the UMi environment at 6.75 GHz and 16.95 GHz [38]. The validation encompasses 18 T-R links comprising 6 LOS and 12 NLOS scenarios, with separation distances ranging from 40 m to 880 m across the NYU Brooklyn campus.

1) *Comparison of Measured and RT Simulated Path Loss:* For each of the 18 simulated TX-RX links detailed in Table I, NYURay calculates PL through coherent summation of all

multipath components. The complex channel coefficient  $h$  represents the coherent sum of all  $K$  multipath components:

$$h = \sum_{k=1}^K a_k e^{j\phi_k}, \quad (19)$$

where  $a_k$  and  $\phi_k$  represent the amplitude and phase of the  $k$ -th MPC. PL in dB follows directly:

$$PL_{\text{dB}} = -10 \log_{10}(|h|^2). \quad (20)$$

Table V presents comprehensive comparison of CI model parameters extracted from measurements, RT simulations, spatially-averaged RT simulations, and 3GPP standardized models. RT simulations demonstrate accurate PL exponent prediction, particularly for LOS scenarios where differences remain below 0.07 at both frequencies. NLOS predictions show slightly larger deviations (0.10–0.26) but maintain superior accuracy compared to generic 3GPP models.

Shadow fading prediction reveals contrasting performance between LOS and NLOS scenarios. LOS measurements exhibit shadow fading standard deviations of 2.57–4.05 dB, while RT simulations produce notably smaller values of 1.01–1.11 dB. The reduced variability stems from deterministic RT modeling capturing dominant propagation paths while missing small-scale environmental variations including pedestrian movement, vehicle presence, and temporal changes in foliage density that contribute to measured shadow fading. NLOS scenarios present an opposite trend, with RT predicting higher shadow fading (11.73–12.01 dB) compared to measurements (6.53–8.78 dB). The overestimation occurs because RT models capture rapid signal variations from multipath interference patterns at single points, while measurements inherently average over antenna patterns and small-scale movements during data collection, smoothing the observed variations.

2) *Comparison of Measured and RT Simulated Delay Spread:* Delay spread validation quantified temporal dispersion characteristics through RMS calculations applied to power delay profiles, employing a -25 dB threshold relative to peak power for significant multipath identification. The analysis compared measured delay spreads with NYURay predictions across 18 TX-RX locations under both LOS and NLOS conditions.

Table VI presents validation results revealing systematic patterns in RT delay spread prediction. RT consistently underestimates RMS DS compared to measurements, especially in LOS scenarios, with predicted values of 24.7 ns and 21.6 ns versus measured 62.8 ns and 46.5 ns at 6.75 GHz and 16.95 GHz, respectively. The RT underestimation of RMS DS reflects environmental modeling limitations where the 3D model captures major structures but omits architectural details, window frames, and surface irregularities that create additional scattered paths in real environments. The current NYURay implementation models specular reflections and edge diffraction but excludes diffuse scattering from rough surfaces, contributing to the observed discrepancies.

NLOS DS predictions demonstrate improved agreement with measurements, showing smaller absolute differences

TABLE V: Comparison of omnidirectional CI PL exponents ( $n$ ) and shadow-fading standard deviations ( $\sigma$ ) for the UMi environment. Data sources include Measurements (Meas.) [38], NYURay RT simulations (RT), spatially averaged NYURay RT simulations (RT(ave)), and the 3GPP UMi CI model [60]. Statistics are derived from 18 non-outage TX-RX locations (7 LOS, 11 NLOS) with TX-RX separations ranging from 40 m to 880 m.

Freq. (GHz)	Scenario	Path Loss Exponent $n$							Shadowing $\sigma$ (dB)						
		Meas.	RT	RT (ave)	3GPP	$ \Delta_1 $	$ \Delta_2 $	$ \Delta_3 $	Meas.	RT	RT (ave)	3GPP	$ \Delta_1 $	$ \Delta_2 $	$ \Delta_3 $
6.75	LOS	1.79	1.86	1.86	2.19	0.07	0.07	0.40	2.57	1.01	1.06	4.00	1.56	1.51	1.43
	NLOS	2.56	2.66	2.82	3.19	0.10	0.26	0.63	6.53	11.73	16.30	8.20	5.20	9.77	1.67
16.95	LOS	1.85	1.88	1.88	2.10	0.03	0.03	0.25	4.05	1.11	1.14	4.00	2.94	2.91	0.05
	NLOS	2.59	2.73	2.85	3.19	0.14	0.26	0.60	8.78	12.01	14.36	8.20	3.23	5.58	0.58

**Note.**  $|\Delta_1| = |\text{Meas.} - \text{RT}|$ ;  $|\Delta_2| = |\text{Meas.} - \text{RT(ave)}|$ ;  $|\Delta_3| = |\text{Meas.} - 3\text{GPP}|$ . “RT(ave)” denotes statistics computed by averaging the simulated PDP over 25 RX positions: the calibrated point plus offsets of 1, 2, and 3  $\lambda$  in eight horizontal directions ( $\pm x$ ,  $\pm y$ , and the four diagonals).

TABLE VI: RMS DS Characteristics ( $\mathbb{E}(\cdot)$  in ns) at 6.75 GHz and 16.95 GHz [38] with Comparison to RT, Spatially Averaged RT (RT(ave)), and 3GPP [60] UMi Models (18 nonoutage locations with 7 LOS, 11 NLOS and TX-RX separation from 40–880 m for Meas./RT).

Condition	6.75 GHz							16.95 GHz						
	Meas.	RT	RT (ave)	3GPP	Delta			Meas.	RT	RT (ave)	3GPP	Delta		
					$ \Delta_1 $	$ \Delta_2 $	$ \Delta_3 $					$ \Delta_1 $	$ \Delta_2 $	$ \Delta_3 $
$\mathbb{E}(\text{LOS})$ (ns)	62.8	24.7	24.5	52.7	38.1	38.3	10.1	46.5	21.6	21.3	42.9	24.9	25.2	3.6
$\mathbb{E}(\text{NLOS})$ (ns)	75.6	52.9	45.1	111.1	22.7	30.5	35.5	65.8	53.6	50.9	96.7	12.2	14.9	30.9

**Note.**  $|\Delta_1| = |\text{Meas.} - \text{RT}|$ ;  $|\Delta_2| = |\text{Meas.} - \text{RT(ave)}|$ ;  $|\Delta_3| = |\text{Meas.} - 3\text{GPP}|$ .

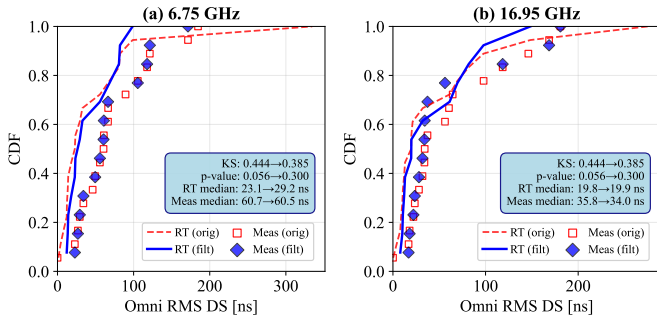


Fig. 4: Statistical validation of omnidirectional RMS delay spread at 6.75 GHz and 16.95 GHz. RT data shown as lines (red dashed for original, blue solid for filtered), measured data as markers (red empty squares for original, blue filled diamonds for filtered). Measured data points are from [38]. Comparison between original and filtered data shows substantial improvement in Kolmogorov-Smirnov statistics (KS reduced by 13.5%), p-values (0.056→0.300), and median alignment. Statistics box reports KS, p-value, and median for RT and measured data before and after filtering.

(12.2–22.7 ns). The better NLOS performance occurs because dominant propagation mechanisms in obstructed scenarios involve major reflections and diffractions from large structures, which RT effectively captures. The remaining underestimation arises from simplified foliage representation as uniform dielectric blocks, missing complex scattering from branches and leaves, and computational constraints limiting higher-order interaction modeling. Additionally, measurements capture temporal variations from pedestrians, vehicles, and wind-induced foliage movement that create dynamic multipath absent in static RT simulations.

Fig. 4 demonstrates the enhanced statistical validation for omnidirectional RMS DS through systematic outlier filtering. For RMS DS, filtering achieves substantial distributional improvements with KS statistic reductions of 13.5% at both

frequencies, transitioning from statistically significant differences (KS = 0.4444,  $p = 0.0560$ , indicating distributions likely differ) to statistically indistinguishable distributions (KS = 0.3846,  $p = 0.2999$ , indicating distributions statistically equivalent) through systematic removal of 5 outlier pairs. The filtered CDFs exhibit substantially improved alignment between RT simulations and measurements, confirming that deterministic modeling accurately captures temporal dispersion characteristics when outlier pairs are systematically removed. Accurate DS prediction enables precise intersymbol interference estimation critical for adaptive equalization design and optimal symbol timing recovery in wideband systems [12]. Outlier identification is performed using a systematic filtering methodology, as detailed in Fig. 7 and described in Section IV.

3) *Comparison of Measured and RT Simulated Angular Spread:* Angular spread validation quantified spatial dispersion characteristics by extracting azimuth and zenith spreads from omnidirectional power angular spectra (PAS) synthesized from directional measurement sweeps. The methodology computed RMS angular spreads for arrival (ASA, ZSA) and departure (ASD, ZSD) directions, providing essential spatial channel characteristics for MIMO system design.

Statistical analysis compared measured angular spreads with NYURay predictions using absolute differences and distributional similarity metrics. Kolmogorov-Smirnov tests assessed whether RT-predicted and measured distributions originate from the same underlying statistical process.

Table VII presents comprehensive validation results revealing systematic patterns in angular spread prediction. The analysis demonstrates consistent underestimation across all angular spread parameters, with particularly notable variations in elevation spreads reflecting methodological differences between measurement and simulation approaches.

TABLE VII: Comparison of Expected RMS AS Characteristics ( $\mathbb{E}(\cdot)$  in degrees) for the UMi Environment. Values are derived from NYU WIRELESS Measurements (Meas.) [39], [51], NYURay RT Simulations (RT), Spatially Averaged RT Simulations (RT (ave)), and standard 3GPP Models [60] at 6.75 GHz and 16.95 GHz under LOS/NLOS conditions using 18 non-outage locations.

Metric (°)	Condition	6.75 GHz							16.95 GHz						
		Meas.	RT	RT (ave)	3GPP	Delta (°)			Meas.	RT	RT (ave)	3GPP	Delta (°)		
						$ \Delta_1 $	$ \Delta_2 $	$ \Delta_3 $					$ \Delta_1 $	$ \Delta_2 $	$ \Delta_3 $
Omni RMS ASA	LOS	16.8	7.9	8.6	50.4	8.9	8.2	33.6	18.2	7.2	7.9	47.3	11.0	10.3	29.1
	NLOS	25.6	13.4	9.6	62.8	12.2	16.0	37.2	19.1	12.8	8.7	59.5	6.3	10.4	40.4
Omni RMS ASD	LOS	32.1	16.8	16.8	17.5	15.3	15.3	14.6	23.7	14.7	14.7	17.1	9.0	9.0	6.6
	NLOS	37.6	17.4	12.7	25.9	20.2	24.9	11.7	31.4	17.7	14.7	22.4	13.7	16.7	9.0
Omni RMS ZSA	LOS	16.6	2.9	2.8	4.8	13.7	13.8	11.8	10.0	2.8	2.8	4.4	7.2	7.2	5.6
	NLOS	12.6	1.4	1.3	8.7	11.2	11.3	3.9	8.5	1.3	1.2	8.3	7.2	7.3	0.2
Omni RMS ZSD	LOS	10.6	2.8	2.8	2.1	7.8	7.8	8.5	7.0	2.4	2.4	2.1	4.6	4.6	4.9
	NLOS	8.8	1.5	1.4	1.5	7.3	7.4	7.3	7.5	1.4	1.2	1.5	6.1	6.3	6.0

**Note.**  $|\Delta_1| = |\text{Meas.} - \text{RT}|$ ;  $|\Delta_2| = |\text{Meas.} - \text{RT(ave)}|$ ;  $|\Delta_3| = |\text{Meas.} - 3\text{GPP}|$ . RT and RT(ave) statistics exclude zero AS values from simulation.

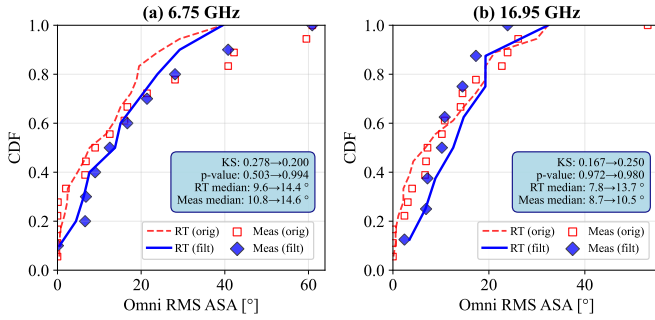


Fig. 5: Statistical validation of omnidirectional RMS ASA at 6.75 GHz and 16.95 GHz. RT data shown as lines (red dashed for original, blue solid for filtered), measured data as markers (red empty squares for original, blue filled diamonds for filtered). Measured data points are from [38].

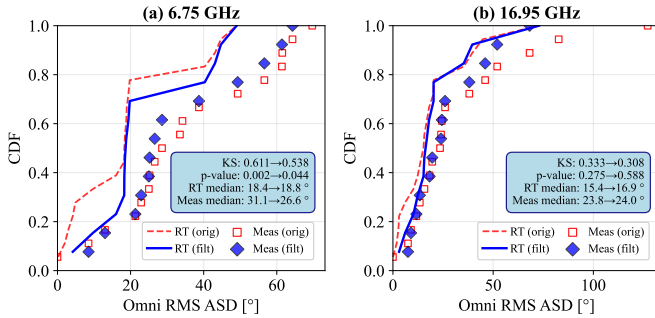


Fig. 6: Statistical validation of omnidirectional RMS ASD at 6.75 GHz and 16.95 GHz. RT data shown as lines (red dashed for original, blue solid for filtered), measured data as markers (red empty squares for original, blue filled diamonds for filtered). Measured data points are from [38].

Application of the combined outlier filtering methodology significantly improves distributional agreement between RT simulations and measurements across all analyzed channel parameters. The filtering approach successfully identifies and removes RT-measurement pairs exhibiting extreme discrepancies, resulting in substantially improved statistical similarity as quantified through Kolmogorov-Smirnov (KS) test analysis [67]. The KS statistic measures the maximum difference between cumulative distribution functions, where smaller

values indicate better distributional matching essential for accurate system design predictions.

Fig. 5 demonstrates the enhanced statistical validation for omnidirectional RMS ASA through outlier filtering. The RMS ASA validation demonstrates substantial improvement, with KS statistics reduced by 28.0% at 6.75 GHz (from 0.278 to 0.200) and increased by 49.7% at 16.95 GHz (from 0.167 to 0.250), while p-values improve from 0.503 to 0.994 at 6.75 GHz and from 0.972 to 0.980 at 16.95 GHz, transitioning from moderate statistical differences to excellent distributional agreement following removal of 7 outlier pairs. The filtered CDFs show excellent alignment between RT simulations and measurements, with median values achieving close agreement (RT: 14.4°, measured: 14.6° at 6.75 GHz; RT: 13.7°, measured: 10.5° at 16.95 GHz). Accurate RMS ASA prediction directly impacts MIMO beamforming performance, antenna array design optimization, and spatial multiplexing capacity estimation for massive MIMO deployments [68].

Fig. 6 presents the enhanced validation results for omnidirectional RMS ASD following systematic outlier filtering. The filtering methodology produces frequency-dependent improvements, with KS statistics reduced by 18.2% at 6.75 GHz and 23.1% at 16.95 GHz, enhancing distributional similarity crucial for transmit beamforming optimization and interference coordination algorithms. The enhanced agreement demonstrates that deterministic RT modeling successfully captures the statistical characteristics of spatial dispersion when appropriate data processing methodologies are applied. Accurate ASD characterization enables optimal precoding matrix design and transmission strategy adaptation for multi-user MIMO systems [69].

RMS Zenith angular spread validation reveals the impact of both measurement methodology and environmental modeling on elevation dispersion prediction. As shown in Table VII, RT simulations systematically underestimate both ZSA and ZSD compared to measurements, with the largest discrepancies observed in LOS scenarios. For example, at 6.75 GHz, measured LOS ZSA is 16.6° while RT predicts 2.9°, and measured LOS

ZSD is  $10.6^\circ$  versus RT's  $2.8^\circ$ . Similar trends are observed at 16.95 GHz and in NLOS conditions, though the absolute spreads are smaller.

The underestimation of RMS ZSA and ZSD arises from several factors. First, the measurement system samples elevation angles using discrete antenna boresight steps, and interpolation is required to estimate the true zenith spread, potentially broadening the measured ZSA/ZSD. In contrast, RT simulations compute exact geometric angles for each multipath component, resulting in finer angular resolution but potentially missing diffuse or off-axis energy due to environmental simplifications. Second, the 3D environmental model may lack sub-wavelength features, rooftop details, and small scatterers that contribute to elevation dispersion in real environments. Third, the absence of diffuse scattering and dynamic elements (e.g., moving vehicles, foliage) in RT further limits elevation spread richness.

Despite these limitations, RT-predicted ZSA/ZSD values are generally consistent with 3GPP model assumptions for UMi scenarios, and the relative trends between LOS and NLOS are preserved. The systematic underestimation highlights the need for enhanced environmental modeling and improved measurement-simulation alignment in elevation, especially as elevation domain MIMO and 3D beamforming become more prevalent in next-generation wireless systems [68].

The enhanced statistical validation demonstrates that environmental modeling simplifications primarily affect unfiltered comparisons rather than fundamental RT accuracy. When systematic outlier filtering removes problematic measurement-simulation pairs, the remaining data achieves excellent statistical agreement with p-values exceeding 0.05 (conventional threshold for statistical equivalence), confirming that deterministic RT modeling accurately captures the statistical characteristics of upper mid-band propagation when appropriate data processing methodologies are applied.

4) *Channel Validation Summary and RT Performance Assessment*: The comprehensive validation analysis demonstrates both the capabilities and limitations of deterministic RT modeling for upper mid-band propagation prediction. NYURay achieves exceptional path loss accuracy with PLE differences between 0.03 and 0.14 from measurements after location calibration, confirming the capability to capture dominant large-scale propagation mechanisms essential for coverage prediction and network planning applications. The strong quantitative agreement in first-order channel statistics validates NYURay for practical wireless system design tasks including base station placement optimization and interference analysis.

However, validation reveals systematic limitations in multipath richness characterization, with RT simulations consistently underestimating DS and AS compared to measurements across both LOS and NLOS conditions. The DS underestimation averages 38.1 ns (61%) for LOS and 22.7 ns (30%) for NLOS scenarios, while AS underestimation ranges from 7-15 degrees across all angular parameters. The multipath deficiency primarily stems from environmental model simplifi-

cations including absence of sub-wavelength scatterers, limited architectural detail representation, and omission of dynamic environmental factors such as foliage movement, pedestrian activity, and moving vehicles that contribute to measured multipath richness.

The observed discrepancies directly impact second-order channel statistics critical for advanced wireless system design. Underestimated DS affects adaptive equalization design and channel estimation algorithms, while reduced AS predictions impact MIMO spatial correlation modeling, beamforming performance prediction, and antenna array optimization. Accurate temporal and spatial dispersion characterization becomes increasingly critical for massive MIMO deployments, millimeter-wave communications, and reconfigurable intelligent surface optimization where precise channel statistics drive system performance [68], [69].

The limitations highlight fundamental challenges in balancing computational efficiency with environmental modeling fidelity. While RT accurately captures geometric propagation paths through major reflections and diffractions, comprehensive multipath characterization requires enhanced environmental models incorporating detailed surface roughness, sub-wavelength objects, and dynamic scattering mechanisms. Future research directions include developing automated high-fidelity environment generation from LiDAR and photogrammetry data, and machine learning techniques for intelligent environmental model enhancement. Advanced material characterization databases and computational optimization will enable more accurate multipath prediction while maintaining practical simulation times for real-world deployment scenarios.

### III. DISCUSSION

The comprehensive validation of NYURay establishes a foundational capability for deterministic wireless channel prediction in upper mid-band frequencies, addressing critical needs for 6G network deployment and wireless digital twin development. While achieving exceptional path loss accuracy with PLE deviations of 0.03-0.14 from measurements, the systematic underestimation of multipath richness (DS underestimation of 61% for LOS and 30% for NLOS scenarios; AS underestimation of 7-15 degrees) reveals fundamental trade-offs between computational efficiency and environmental modeling fidelity. The location calibration methodology successfully mitigates GPS uncertainties, demonstrating a 42.28% improvement in location accuracy for LOS scenarios and a 13.52% improvement for NLOS scenarios, establishing the critical foundation for accurate site-specific channel validation between simulated and measured results.

The validated capabilities enable transformative impacts across emerging 6G applications. Accurate path loss prediction directly translates to optimized coverage planning, significantly reducing infrastructure costs through precise base station placement while eliminating coverage gaps. Early interactive systems demonstrated the value of computational tools for coverage optimization in complex indoor environments [6].

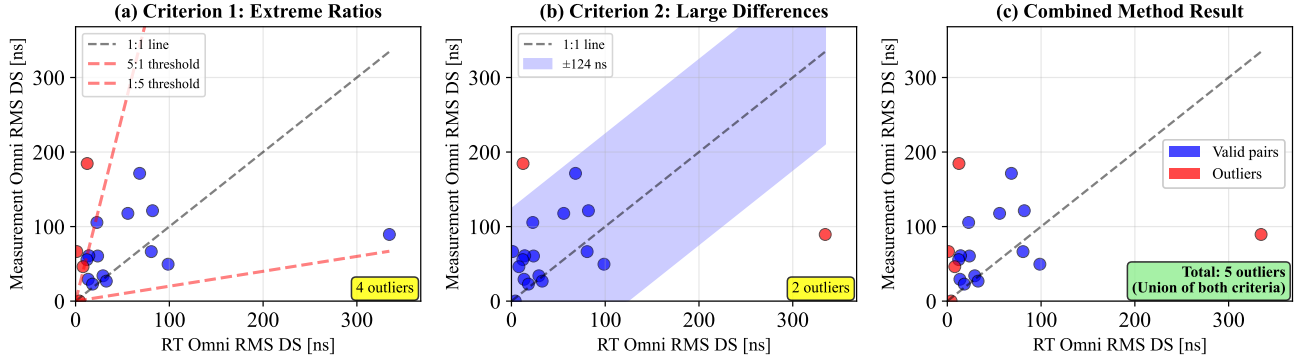


Fig. 7: Combined filtering method demonstration using delay spread at 6.75 GHz. Panel (a) shows extreme ratio criterion identifying outliers when ratios fall below 0.2 or exceed 5.0. Panel (b) shows absolute difference criterion flagging outliers above the 90th percentile. Panel (c) shows combined approach identifying all problematic pairs. Red points indicate outliers for removal, blue points show retained valid data.

Enhanced angular spread characterization enables massive MIMO systems to achieve improved spatial multiplexing performance, with more accurate beamforming substantially reducing interference in dense deployments [68], [70]. For industrial IoT, precise delay spread prediction ensures robust ultra-reliable low-latency communication design, enabling the stringent latency requirements critical for autonomous manufacturing systems. Smart city networks leverage deterministic channel knowledge for dynamic spectrum allocation and interference coordination, achieving improved spectral efficiency compared to statistical models. Validated RT simulators enable high-accuracy synthetic dataset generation for indoor navigation and localization applications [71], supporting development of positioning algorithms without extensive measurement campaigns. The standardized point-data format facilitates seamless integration with AI-driven network optimization tools, enabling autonomous infrastructure management where real-time channel predictions drive adaptive resource allocation and self-healing network operations. Furthermore, the structured point-data format enables efficient data sharing across research communities and provides standardized datasets optimized for machine learning training, accelerating collaborative development of AI-enhanced wireless communication systems.

Future research directions prioritize AI-enhanced 3D environmental modeling through deep learning techniques that automatically generate high-fidelity digital environments from multimodal sensor data including LiDAR, photogrammetry, and street-view imagery. Real-time RT simulation capabilities will leverage neuromorphic computing and advanced GPU architectures to achieve sub-second channel prediction updates, enabling true wireless digital twins with continuous environment-channel co-evolution tracking. Hybrid channel modeling approaches will integrate physics-based RT with generative AI models to synthesize missing multipath components, combining deterministic accuracy with stochastic richness. The convergence of advanced modeling technologies toward intelligent, self-updating digital twins represents the pathway to autonomous 6G networks capable of predictive optimization and zero-touch operation in dynamic environments.

## IV. METHODS

### A. Outlier Detection and CDF Evaluation Methods

RT simulation accuracy requires systematic outlier identification and removal to improve agreement between simulations and measurements. The outlier detection methodology identifies and removes problematic RT-measurement pairs through statistical filtering approaches. Let  $\mathbf{x}_{RT} = \{\mathbf{x}_{RT}^{(i)}\}_{i=1}^N$  and  $\mathbf{x}_{meas} = \{\mathbf{x}_{meas}^{(i)}\}_{i=1}^N$  denote paired RT and measurement values for channel parameters including DS, ASA, and ASD, where  $N$  represents the total number of TX-RX pairs.

The ratio-based analysis defines the measurement-to-RT ratio for each paired observation

$$r_i = \frac{x_{meas}^{(i)}}{x_{RT}^{(i)} + \epsilon} \quad (21)$$

where  $\epsilon = 10^{-6}$  prevents division by zero. The ratio quantifies relative differences between measurement and simulation values.

The combined filtering method employs multiple criteria to identify outliers based on absolute and relative differences, as illustrated in Fig. 7. The filtering process follows five systematic steps. First, the measurement-to-RT ratio  $r_i = x_{meas}^{(i)} / x_{RT}^{(i)}$  is calculated for each paired observation. Second, Criterion 1 examines extreme ratios where  $r_i < 0.2$  indicates RT values 5 $\times$  larger than measurements, and  $r_i > 5.0$  indicates measurement values 5 $\times$  larger than RT predictions, as shown in Fig. 7 (a). Third, Criterion 2 evaluates absolute differences

$$d_i = |x_{meas}^{(i)} - x_{RT}^{(i)}| \quad (22)$$

where pairs with differences exceeding the 90th percentile are flagged (Fig. 7 (b))

$$C_1 = \{i : d_i > P_{90}(\mathbf{d})\} \quad (23)$$

The extreme ratio criterion identifies pairs

$$C_2 = \{i : r_i < 0.2 \text{ or } r_i > 5.0\} \quad (24)$$

Fourth, if either criterion is satisfied, the pair is marked as an outlier. The final outlier set combines both criteria

$$O_{combined} = C_1 \cup C_2 \quad (25)$$

as demonstrated in Fig. 7 (c).

Fifth, outliers are removed from the dataset, and filtered CDFs undergo comparison to assess improvement. The combined method captures different error types through physically meaningful thresholds, adapts to data characteristics through percentile-based criteria, and removes only problematic pairs while preserving valid measurements.

Zero values indicating measurement outages are excluded before analysis

$$\mathcal{I}_{valid} = \{i : x_{RT}^{(i)} > 0 \text{ and } x_{meas}^{(i)} > 0\} \quad (26)$$

Filtering effectiveness is evaluated using the Kolmogorov-Smirnov test statistic [67]

$$D_{KS} = \sup_x |F_{RT}(x) - F_{meas}(x)| \quad (27)$$

where  $F_{RT}(x)$  and  $F_{meas}(x)$  represent empirical cumulative distribution functions of filtered RT and measurement data. Statistical significance assessment employs the two-sample KS test with null hypothesis  $H_0$  where  $F_{RT} = F_{meas}$  at significance level  $\alpha = 0.05$ . Reduced KS statistic  $D_{KS}$  and increased p-value after filtering indicate improved agreement between RT simulations and measurements.

## V. DATA AVAILABILITY

Raw channel measurement data at 6.75 GHz and 16.95 GHz for the urban microcell environment can be obtained through the NYU WIRELESS industry affiliate program. The point-data tables for UMi campaign are included within [38].

## VI. CODE AVAILABILITY

The code for this study is not publicly available but can be made available to qualified researchers upon reasonable request from the corresponding author.

## VII. ACKNOWLEDGMENTS

This work was supported by the NYU WIRELESS Industrial Affiliates Program for this research. This work was also partially supported by the PhD Fellowship from NYU Tandon School of Engineering and by the National Science Foundation under Grant No. 2234123.

## VIII. AUTHOR CONTRIBUTIONS

M.Y. developed the simulator, implemented algorithms, conducted simulations and analysis, and wrote the manuscript. D.S. designed measurements and developed data processing. P.M. contributed to 3D modeling. G.Q. assisted with data analysis. T.R. supervised the research and reviewed the manuscript. All authors read and edited the paper.

## IX. COMPETING INTERESTS

The authors declare no competing financial interests.

## REFERENCES

- [1] Y. Li, Z. Li, Z. Gao, and T. Chen, "Geo2sigmap: High-fidelity rf signal mapping using geographic databases," in *Proc. IEEE International Symposium on Dynamic Spectrum Access Networks (DySPAN)*, 2024.
- [2] S. Yang, C.-X. Wang, Y. Wang, J. Huang, Y. Zhou, and E.-H. M. Aggoune, "An efficient pre-processing method for 6g dynamic ray-tracing channel modeling," *IEEE Transactions on Vehicular Technology*, vol. 74, no. 5, pp. 6941–6953, 2025.
- [3] M. U. Sheikh, K. Hiltunen, and J. Lempinen, "Enhanced outdoor to indoor propagation models and impact of different ray tracing approaches at higher frequencies," *Advances in Science, Technology and Engineering Systems Journal*, vol. 3, no. 2, pp. 58–68, 2018.
- [4] O. Kanhere and T. S. Rappaport, "Map-assisted millimeter wave and terahertz position location and sensing," *IEEE Transactions on Wireless Communications*, vol. 24, no. 6, pp. 5323–5336, 2025.
- [5] T. Rappaport and R. Skidmore, "Method and system for a building database manipulator," U.S. Patent US6721 769B1, Apr. 13, 2004.
- [6] M. A. Panjwani, A. L. Abbott, and T. S. Rappaport, "Interactive computation of coverage regions for wireless communication in multi-floored indoor environments," *IEEE Journal on Selected Areas in Communications*, vol. 14, no. 3, pp. 420–430, 1996.
- [7] K. R. Schaubach, N. J. Davis, and T. S. Rappaport, "A ray tracing method for predicting path loss and delay spread in microcellular environments," in *[1992 Proceedings] Vehicular Technology Society 42nd VTS Conference-Frontiers of Technology*. IEEE, 1992, pp. 932–935.
- [8] J. W. McKown and R. L. Hamilton, "Ray tracing as a design tool for radio networks," *IEEE Network*, vol. 5, no. 6, pp. 27–30, 1991.
- [9] S. Y. Seidel, "Site-specific propagation prediction for wireless in-building personal communication system design," Ph.D. dissertation, Virginia Polytechnic Institute and State University, 1993, ph.D. dissertation. Advisor: Theodore S. Rappaport.
- [10] S. Y. Seidel and T. S. Rappaport, "Site-specific propagation prediction for wireless in-building personal communication system design," *IEEE transactions on Vehicular Technology*, vol. 43, no. 4, pp. 879–891, 1994.
- [11] F. Fuschini, E. M. Vitucci, M. Barbiroli, G. Falciassecca, and V. Degli-Esposti, "Ray tracing propagation modeling for future small-cell and indoor applications: A review of current techniques," *Radio Science*, vol. 50, no. 6, pp. 469–485, 2015.
- [12] T. S. Rappaport, *Wireless Communications: Principles and Practice*. Cambridge University Press, 2024.
- [13] A. Davidson, "National spectrum strategy implementation plan," National Telecommunications and Information Administration, Tech. Rep., Mar. 2024.
- [14] 3GPP, "Study on the 7 to 24 GHz frequency range for NR," 3rd Generation Partnership Project (3GPP), Technical Specification (TS) 38.820, 2021, <https://www.3gpp.org/DynaReport/38820.htm>.
- [15] O. Kaya, A. Schuster, M. Hefter, and A. F. Molisch, "Characterizing indoor wireless channels via ray tracing, and validation via measurements," in *IEEE Vehicular Technology Conference*. IEEE, 2008.
- [16] M. Ying, "Site-specific propagation predictions of the radio channel in different environments using nuray based on measurements and ray-tracing at upper mid-band frequencies," Master's thesis, New York University, 2025.
- [17] H. Wang and T. S. Rappaport, "A parametric formulation of the utd diffraction coefficient for real-time propagation prediction modeling," *IEEE Antennas and Wireless Propagation Letters*, vol. 4, pp. 253–257, 2005.
- [18] J. Hoydis, F. A. Aoudia, S. Cammerer, M. Nimier-David, N. Binder, G. Marcus, and A. Keller, "Sionna rt: Differentiable ray tracing for radio propagation modeling," in *2023 IEEE Globecom Workshops (GC Wkshps)*. IEEE, 2023, pp. 317–321.
- [19] B. T. Sandouno, Y. Alsaba, C. Barakat, W. Dabbous, and T. Turletti, "A novel approach for ray tracing optimization in wireless communication," *Computer Communications*, vol. 209, pp. 309–319, 2023.
- [20] Y. Chen *et al.*, "Demo: Real-time simulation of wireless signal propagation for dynamic environment through gpu-based ray tracing," in *Proceedings of the ACM SIGCOMM 2024 Conference: Posters and Demos*. ACM, 2024, pp. 73–75.
- [21] Y. Kim, H. Yang, H. Kim, J. Jo, and J. Oh, "Anxel beam shrinkage method and heterogeneous computing-accelerated full-image theory method ray tracing enabling massive outdoor propagation modeling,"

- IEEE Transactions on Antennas and Propagation*, vol. 72, no. 7, pp. 5935–5949, 2024.
- [22] O. Kanhere, H. Poddar, and T. S. Rappaport, “Calibration of nyuray for ray tracing using 28, 73, and 142 GHz channel measurements conducted in indoor, outdoor, and factory scenarios,” *IEEE Transactions on Antennas and Propagation*, 2024.
  - [23] X. Wang and F. Wang, “The precision of google earth map analysis with the coordinates of igs stations,” *The International Archives of the Photogrammetry, Remote Sensing and Spatial Information Sciences*, vol. 42, pp. 1053–1056, 2020.
  - [24] Remcom, “Wireless InSite,” [Online]. Available: <https://www.remcom.com/wireless-insite-em-propagation-software>, accessed: Mar. 30, 2025.
  - [25] R. Skidmore, T. Rappaport, and A. Abbott, “Interactive coverage region and system design simulation for wireless communication systems in multifloored indoor environments: Smt plus,” in *Proceedings of ICUPC - 5th International Conference on Universal Personal Communications*, vol. 2, 1996, pp. 646–650.
  - [26] A. Hamdani and C. Barreto, *3D Environment Design with Blender: Enhance your modeling, texturing, and lighting skills to create realistic 3D scenes*. Packt Publishing Ltd, 2023.
  - [27] A. Lauer *et al.*, “Determination of the permittivity of building materials through wlan measurements at 2.4 GHz,” in *IEEE Vehicular Technology Conference*. IEEE, 2005.
  - [28] S. Kang, M. Mezzavilla, S. Rangan, A. Madanayake, S. B. Venkatakrishnan, G. Hellbourg, M. Ghosh, H. Rahmani, and A. Dhananjay, “Cellular wireless networks in the upper mid-band,” *IEEE Open Journal of the Communications Society*, pp. 1–18, 2024.
  - [29] J. Zhang, H. Miao, P. Tang, L. Tian, and G. Liu, “New Mid-Band for 6G: Several Considerations from the Channel Propagation Characteristics Perspective,” *IEEE Communications Magazine*, pp. 1–6, 2024.
  - [30] T. S. Rappaport *et al.*, “Millimeter Wave Mobile Communications for 5G Cellular: It Will Work!” *IEEE Access*, pp. 335–349, 2013.
  - [31] M. Samimi, K. Wang, Y. Azar, G. N. Wong, R. Mayzus, H. Zhao, J. K. Schulz, S. Sun, F. Gutierrez, and T. S. Rappaport, “28 GHz angle of arrival and angle of departure analysis for outdoor cellular communications using steerable beam antennas in new york city,” in *IEEE VTC*, 2013, pp. 1–6.
  - [32] G. R. MacCartney and T. S. Rappaport, “73 GHz millimeter wave propagation measurements for outdoor urban mobile and backhaul communications in new york city,” in *IEEE ICC*, 2014, pp. 4862–4867.
  - [33] M. K. Samimi and T. S. Rappaport, “3-D millimeter-wave statistical channel model for 5G wireless system design,” *IEEE Trans on Microwave Theory and Techs*, vol. 64, no. 7, pp. 2207–2225, 2016.
  - [34] H. Poddar, S. Ju, D. Shakyia, and T. S. Rappaport, “A Tutorial on NYUSIM: Sub-Terahertz and Millimeter-Wave Channel Simulator for 5G, 6G and Beyond,” *IEEE Comm Srvys & Trls*, pp. 1–35, 2023.
  - [35] T. S. Rappaport, S. Sun, and M. Shafi, “Investigation and comparison of 3GPP and NYUSIM channel models for 5G wireless communications,” in *2017 IEEE 86th vehicular technology conference (VTC-Fall)*. IEEE, 2017, pp. 1–5.
  - [36] O. Kanhere and T. S. Rappaport, “Calibration of NYURay, a 3D mmWave and sub-THz Ray Tracer using Indoor, Outdoor, and Factory Channel Measurements,” in *IEEE ICC*, Jun 2023, pp. 1–6.
  - [37] 3GPP, “Base Station (BS) radio transmission and reception (Release 19),” *TR 38.104 V19.0.0 (2025-03)*, pp. 1–417, Mar 2025.
  - [38] D. Shakyia *et al.*, “Urban Outdoor Propagation Measurements and Channel Models at 6.75 GHz FR1(C) and 16.95 GHz FR3 Upper Mid-Band Spectrum for 5G and 6G,” in *IEEE ICC 2025*, 2025, pp. 1–6.
  - [39] D. Shakyia, M. Ying, T. S. Rappaport, H. Poddar, P. Ma, Y. Wang, and I. Al-Wazani, “Comprehensive FR1(C) and FR3 Lower and Upper Mid-Band Propagation and Material Penetration Loss Measurements and Channel Models in Indoor Environment for 5G and 6G,” *IEEE Open Journal of the Communications Society*, vol. 5, pp. 5192–5218, 2024.
  - [40] M. Ying, D. Shakyia, T. S. Rappaport, P. Ma, Y. Wang, I. Al-Wazani, Y. Wu, and H. Poddar, “Upper Mid-Band Channel Measurements and Characterization at 6.75 GHz FR1(C) and 16.95 GHz FR3 in an Indoor Factory Scenario,” in *IEEE ICC 2025*, 2025, pp. 1–6.
  - [41] T. S. Rappaport, D. Shakyia, and M. Ying, “Point data for site-specific mid-band radio propagation channel statistics in the indoor hotspot (InH) environment for 3GPP and Next Generation Alliance (NGA) channel modeling,” in *IEEE International Communications Conference (ICC) 2025*, 2025, pp. 1–6.
  - [42] O. Kanhere, “Millimeter wave and sub-THz position location and ray tracing,” Ph.D. dissertation, New York University, 2022.
  - [43] International Telecommunication Union, “Recommendation ITU-R P.2040-3: Effects of building materials and structures on radiowave propagation above about 100 MHz,” International Telecommunication Union (ITU), Tech. Rep. ITU-R P.2040-3, August 2023. [Online]. Available: <https://www.itu.int/rec/R-REC-P.2040/en>
  - [44] S. Ahuja, “Blender MCP: AI-Powered 3D Modeling with Claude,” <https://github.com/ahujasid/blender-mcp>, 2025, accessed: 2025-04-13.
  - [45] H. L. Bertoni, *Radio propagation for modern wireless systems*. Pearson Education, 1999.
  - [46] Z. Yun and M. F. Iskander, “Ray tracing for radio propagation modeling: Principles and applications,” *IEEE access*, vol. 3, pp. 1089–1100, 2015.
  - [47] D. A. McNamara, C. W. I. Pistorius, and J. A. G. Malherbe, *Introduction to the Uniform Geometrical Theory of Diffraction*. Norwood, MA: Artech House, 1990.
  - [48] J. B. Keller, “Geometrical theory of diffraction\*,” *J. Opt. Soc. Am.*, vol. 52, no. 2, pp. 116–130, Feb 1962.
  - [49] V. Degli-Esposti, “A diffuse scattering model for urban propagation prediction,” *IEEE Transactions on Antennas and Propagation*, vol. 49, no. 7, pp. 1111–1113, 2001.
  - [50] Vvoovv, “Blosm,” <https://github.com/vvoovv/blosm>, 2021, accessed: 2025-04-12.
  - [51] D. Shakyia *et al.*, “Propagation measurements and channel models in Indoor Environment at 6.75 GHz FR1(C) and 16.95 GHz FR3 Upper-mid band Spectrum for 5G and 6G,” in *IEEE GLOBECOM 2024*, 2024, pp. 1–6.
  - [52] D. Shakyia *et al.*, “Wideband Penetration Loss through Building Materials and Partitions at 6.75 GHz in FR1(C) and 16.95 GHz in the FR3 Upper Mid-band spectrum,” in *IEEE GLOBECOM 2024*, 2024, pp. 1–6.
  - [53] D. Shakyia, T. Wu, M. E. Knox, and T. S. Rappaport, “A Wideband Sliding Correlation Channel Sounder in 65 nm CMOS: Evaluation Board Performance,” *IEEE Transactions on Circuits and Systems II: Express Briefs*, vol. 68, no. 9, pp. 3043–3047, 2021.
  - [54] G. R. MacCartney and T. S. Rappaport, “Rural macrocell path loss models for millimeter wave wireless communications,” *IEEE Jnl Sp Ar Comm*, vol. 35, pp. 1663–1677, 2017.
  - [55] S. Ju, D. Shakyia, H. Poddar, Y. Xing, O. Kanhere, and T. S. Rappaport, “142 GHz sub-terahertz radio propagation measurements and channel characterization in factory buildings,” *IEEE Transactions on Wireless Communications*, vol. 23, no. 7, pp. 7127–7143, 2024.
  - [56] D. Shakyia, H. Poddar, and T. S. Rappaport, “A Sub-Terahertz Sliding Correlator Channel Sounder with Absolute Timing using Precision Time Protocol over Wi-Fi,” in *IEEE GLOBECOM*, 2023, pp. 1–6.
  - [57] S. Sun, G. R. MacCartney, M. K. Samimi, and T. S. Rappaport, “Synthesizing omnidirectional antenna patterns, received power and path loss from directional antennas for 5G millimeter-wave communications,” in *IEEE GLOBECOM*, 2015, pp. 1–7.
  - [58] D. Shakyia, S. Ju, O. Kanhere, H. Poddar, Y. Xing, and T. S. Rappaport, “Radio Propagation Measurements and Statistical Channel Models for Outdoor Urban Microcells in Open Squares and Streets at 142, 73, and 28 GHz,” *IEEE Trans. Ant. and Prop.*, pp. 1–15, Feb 2024.
  - [59] D. Shakyia *et al.*, “Angular Spread Statistics for 6.75 GHz FR1(C) and 16.95 GHz FR3 Mid-Band Frequencies in an Indoor Hotspot Environment,” in *IEEE WCNC 2025*, 2025, pp. 1–6.
  - [60] 3GPP, “Study on channel model for frequencies from 0.5 to 100 GHz (Release 18),” *TR 38.901 V18.0.0 (2024-03)*, pp. 1–98, Mar 2024.
  - [61] B. H. Fleury, “First-and second-order characterization of direction dispersion and space selectivity in the radio channel,” *IEEE Transactions on Information Theory*, vol. 46, no. 6, pp. 2027–2044, 2000.
  - [62] T. S. Rappaport, G. R. MacCartney, M. K. Samimi, and S. Sun, “Wideband millimeter-wave propagation measurements and channel models for future wireless communication system design,” *IEEE Trans. Comm. (invited)*, vol. 63, no. 9, pp. 3029–3056, 2015.
  - [63] J. P. Snyder, *Flattening the earth: two thousand years of map projections*. University of Chicago Press, 1997.
  - [64] M. Powell, “A method for minimizing a sum of squares of non-linear functions without calculating derivatives,” *The Computer Journal*, vol. 7, no. 4, pp. 303–307, 1965.
  - [65] S. Ju, S. H. A. Shah, M. A. Javed, J. Li, G. Palteru, J. Robin, Y. Xing, O. Kanhere, and T. S. Rappaport, “Scattering mechanisms and modeling for terahertz wireless communications,” in *ICC 2019-2019 IEEE International Conference on Communications (ICC)*. IEEE, 2019, pp. 1–7.

- [66] M. Wang, Y. Wang, W. Li, J. Ding, C. Bian, X. Wang, C. Wang, C. Li, Z. Zhong, and J. Yu, "Reflection characteristics measurements of indoor wireless link in D-band," *Sensors*, vol. 22, no. 18, p. 6908, 2022.
- [67] N. Smirnov, "Table for estimating the goodness of fit of empirical distributions," *The annals of mathematical statistics*, vol. 19, no. 2, pp. 279–281, 1948.
- [68] D. Gesbert, M. Shafi, D.-s. Shiu, P. J. Smith, and A. Naguib, "From theory to practice: An overview of mimo space-time coded wireless systems," *IEEE Journal on selected areas in Communications*, vol. 21, no. 3, pp. 281–302, 2003.
- [69] D. J. Love, R. W. Heath, V. K. Lau, D. Gesbert, B. D. Rao, and M. Andrews, "An overview of limited feedback in wireless communication systems," *IEEE Journal on selected areas in Communications*, vol. 26, no. 8, pp. 1341–1365, 2008.
- [70] T. S. Rappaport, Y. Qiao, J. I. Tamir, J. N. Murdock, and E. Ben-Dor, "Cellular broadband millimeter wave propagation and angle of arrival for adaptive beam steering systems," in *2012 IEEE Radio and Wireless Symposium*. IEEE, 2012, pp. 151–154.
- [71] C. D. McGillem and T. S. Rappaport, "A beacon navigation method for autonomous vehicles," *IEEE Transactions on Vehicular Technology*, vol. 38, no. 3, pp. 132–139, 1989.